Journal of Energy Chemistry 62 (2021) 431–439

Contents lists available at ScienceDirect

Journal of Energy Chemistry

journal homepage: www.elsevier.com/locate/jechem

http://www.journals.elsevier.com/journal-of-energy-chemistry/

Magnesium hydride nanoparticles anchored on MXene sheets as high capacity anode for lithium-ion batteries

Shulin Zhong [a], Shunlong Ju [a], Yifei Shao [b], Wei Chen [a], Tengfei Zhang [b], Yuqin Huang [c], Hongyu Zhang [a], Guanglin Xia [a], Xuebin Yu [a,*]

[a] Department of Materials Science, Fudan University, Shanghai 200433, China
[b] Jiangsu Key Laboratory of Electrochemical Energy-Storage Technologies, College of Materials Science and Technology, Nanjing University of Aeronautics and Astronautics, Nanjing 210016, Jiangsu, China
[c] Institute for Superconducting and Electronic Materials, University of Wollongong, Wollongong, NSW 2522, Australia

ARTICLE INFO

Article history:
Received 5 March 2021
Revised 24 March 2021
Accepted 26 March 2021
Available online 6 April 2021

Keywords:
Lithium ion batteries
Magnesium hydrides
MXene sheets

ABSTRACT

Magnesium hydride, with high specific capacity, favorable voltage profile and low voltage hysteresis properties, is regarded as a promising anode for lithium storage. However, the rapid fading of capacity caused by huge volume change, low electron/ion conduction, and spontaneous agglomeration of active materials during cycling greatly limit its practical application in lithium-ion batteries. Herein, we report the synthesis of monodisperse MgH_2 nanoparticles with an average particle size of <20 nm homogeneously anchored on Ti_3C_2 MXene sheets by bottom-up self-assembly strategy. The unique nanoarchitectures are able to efficiently enhance the lithium insertion/extraction kinetics, accelerate the electron/lithium ion transfer and buffer the strain of volume changes. More importantly, the formed F–Mg bounding between MgH_2 and MXene could avoid the shedding of MgH_2 nanoparticles to electrolyte during cycling, which significantly enhance the capacity, cyclability, and rate performance of magnesium hydride. Moreover, due to the high density of MXene and the synergistic effect between the MgH_2 and MXene matrix, the MgH_2/MXene composite with 60 wt% MgH_2 delivers a superior volumetric capacity of 1092.9 mAh cm^{-3} at a current density of 2000 mA g^{-1} after 1000 cycles. These results highlight the great promising of MgH_2/MXene composite for high performance lithium-ion batteries.

Introduction

The rapidly increased demand of lithium ion batteries (LIBs) has given rise to social demand for anode materials of LIBs with high electrochemical performance that can deliver and accumulate higher energy density. However, the current commercial graphite anode only has a limited capacity of 372 mAh g^{-1} [1], which is far from the requirement of high energy LIBs. Consequently, a number of promising anode materials such as metals [2,3], semiconductors [4,5], metal oxides [6,7], sulfides [8,9], carbides [10,11], phosphides [12,13], metal hydrides [14,15], and so forth [16,17] have been explored for LIBs. Among which, magnesium hydride as one of the typical metal hydrides has been firstly proposed by Oumellal et al. [18] as a prospective anode materials for LIBs in 2008 due to its attractive theoretical capacity (2038 mAh g^{-1}, 2878 mAh cm^{-3}), low platform and voltage hysteresis, and abundant supply of raw materials in nature. Nevertheless, the practical application of MgH_2 is hindered largely by its low conductive, slow transportation of Li ion, sluggish reaction dynamic, and extremely inevitable volume expansion/shrinkage during lithium insertion/extraction process, which will cause the instability of solid electrolyte interface (SEI), the pulverization of electrode during working, and eventually severe fading of capacity upon cycling [19,20].

To address the above issues, tremendous strategies have been made to improve the electrochemical performance of MgH_2, including reducing the particle size of MgH_2 to shorten the transmission path of Li^+ [21,22], combining MgH_2 nanoparticles with graphene to prevent the aggregation of MgH_2 nanoparticles, buffering the volume change and enhance the conductivity of battery system [23], coating the MgH_2 nanoparticles by conductive polymer to stabilize the formed SEI film [24]. For instance, Oumellal et al. [22] reported the synthesis of MgH_2/porous carbon composite by bottom-up method and the composite delivered a reversible capacity of 500 mAh g^{-1} after 25 cycles at

* Corresponding author.
E-mail address: yuxuebin@fudan.edu.cn (X. Yu).

https://doi.org/10.1016/j.jechem.2021.03.049

100 mA g^{-1}. Recently, a MgH_2/graphene composite was synthesized by solvothermal method [23], in which graphene could not only efficiently prevent the aggregation of active material, but also buffer the volume changes in the process of repeated discharge/charge. As a result, a reversible high capacity of 946 mAh g^{-1} was achieved by the composite after 100 cycles at 100 mA g^{-1}. Furthermore, a core–shell structured polythiophene-coated MgH_2 on graphene (G/MgH_2@PTh) composite has attracted extensive attention because of its unique structure [24]. Such a nanoarchitecture could efficiently enhance the stability of SEI layer by PTh shell and thus providing a high specific lithium storage capacity of 1311 mAh g^{-1} after 100 cycles at 100 mA g^{-1}. The above results indicate that carbon-based materials, particularly graphene, are idea templates to load MgH_2 with improved electrochemical performance and enhanced gravimetric capacity. However, the volumetric capacity is also a non-negligible index to estimate the performance of electrode material in battery system. Carbon-based materials, due to their natural light feature, are obviously unfavorable to enhance the volumetric capacity of MgH_2.

Recently, two-dimensional (2D) transitional metal carbides/nitrides with a designation of MXene have been attracted a great of attention in supercapacitors [25–27], LIBs [28,29], Na-ion batteries [30,31], Li-O_2 batteries [32,33], because of their rich surface functional groups (–O, –OH, –F) [34], highly hydrophilic surface, and tunable properties without sacrificing the metal conductive. Compared with carbon-based materials, MXene sheets have additional benefits as both the active or matrix materials. For example, MXene based electrode could operate at high current density owing to the preeminent pseudocapacitive behavior of MXene [35]. More importantly, MXene favors to supply a high volumetric energy density because of its natural high density. For instance, free-standing MXene papers with density of 3–4 g cm^{-3} can provide a high volumetric capacity that is several times larger than that of graphene [25,36,37]. In addition, PVP-Sn(IV)@MXene composite was reported to deliver a superior reversible volumetric capacity of 1375 mAh cm^{-3} at 100 mA g^{-1} after 50 cycles [38]. More recently, a high volumetric capacity of 2460 mAh cm^{-3} at 200 mA g^{-1} was reported by a η-MoC/MXene/C composite after 300 cycles [39]. These attractive results suggest the potential application prospect of MXene as template to load MgH_2 with enhanced volumetric energy density for LIBs.

Herein, combining the merits of MgH_2 and MXene in LIBs, we fabricated the composites of nanostructured MgH_2 anchored on MXene sheets (named as nMH/MX) by bottom-up self-assembly method. The nMH/MX composites exhibit four distinguishing features as anode of LIBs (i) monodisperse MgH_2 nanoparticles with an average diameter of <20 nm were well loaded on MXene, which can shorten the pathway of electron/lithium ion transportation, and further enhancing the lithium insertion/extraction kinetics of MgH_2; (ii) F–Mg bounding was formed between MXene and MgH_2, which is able to prevent the shedding of MgH_2 nanoparticles to electrolyte during cycling; (iii) MXene sheets with flexibility could efficiently buffer the strain caused by volume change during cycling and further avoid the pulverization of active materials; (iv) 2D MXene network could also accelerate the lithium ion/electron transfer and provide part of capacity for the whole electrode. As a result, the obtained nMH/MX composites display outstanding electrochemical performance with largely enhanced cycling stability, superior volumetric capacity, and excellent rate performance.

Experimental

Preparation of Ti_3C_2 MXene

To prepare Ti_3C_2 MXene, 0.5 g Ti_3AlC_2 (11 Technology Co., Ltd.) was etched in a mixture solution containing 0.5 g LiF and 10 mL 9 M hydrochloric acid for 24 h at 35 °C. The products were washed by centrifugation with deionized (DI) water until the pH > 6. Afterwards, the obtained materials were redispersed in water and subsequently sonicated for 2 h at 10 °C under continuous Ar bubbling. The sonicated suspension was then centrifuged at 3500 r min^{-1} for 1 h to obtain the dark green MXene suspension. To load MgH_2, MXene suspension was freeze-dried and subsequently calcined at 600 °C for 2 h with 5 °C min^{-1} heating rate under Ar.

Preparation of MgH_2-based materials

The nMH/MX composites with various MgH_2 contents were fabricated by the hydrogenation of dibutyl magnesium ($MgBu_2$) in cyclohexane (C_6H_{12}). Briefly, 1.6 mL 1 M $MgBu_2$ in heptane and a certain amount of MXene (see Table S1) were mixed in 40 mL cyclohexane in a pressure reactor vessel. Afterwards, the reactor was filled with hydrogen until the pressure achieved 4.5 MPa and subsequently heated to 200 °C for 24 h under vigorous stirring. Finally, the reacted suspension was centrifuged and dried at 70 °C via dynamic vacuum on a Schlenk line. nMH/MX composites with a nMH content of 20, 40, 60 and 80 wt% were signed as nMH/MX-20, nMH/MX-40, nMH/MX-60 and nMH/MX-80, respectively. nMHs were synthesized by the similar method without MXene matrix. The cMH/MX-60 and cMH/C-60 composites were synthesized by ball-milling 60 wt% cMH with MXene and Super P, respectively, under Ar atmosphere for 8 h with 1:30 ball-to-powder ratio and 350 r min^{-1} rotation speed.

Computational details

Density functional theory (DFT) calculations were carried out using projector-augmented wave (PAW) method as implemented in Vienna *ab initio* simulation package (VASP). A generalized gradient approximation (GGA) of Perdew-Burke-Ernzerhof (PBE) functional was employed to describe the exchange–correlation interaction. A 3 × 3 supercell of Ti_3C_2 MXene was used, and a void region of 20 Å was included in the direction perpendicular to the MXene plane. To ensure the accuracy of the calculated results, the energy cutoff was set to 520 eV and the Brillouin zone was sampled by 9 × 9 × 1 Monkhorst-Pack *k*-points mesh in all calculations. The DFT-D3 method was also adopted to evaluate the van der Waals interactions. The structures were relaxed until the forces and total energy on all atoms were converged to less than 0.05 eV $Å^{-1}$ and 1 × 10^{-5} eV. The charge difference plots are obtained by subtracting the charge densities of pristine F-Ti_3C_2 and isolated MgH_2 molecule from that of MgH_2 adsorbed F-Ti_3C_2.

To evaluate the adhesive strength of MgH_2, the binding energy (E_b) was calculated for every MgH_2 adsorbed compound. E_b was defined as the energy difference before and after MgH_2 adsorption,

$$E_b = E_{total} - E_{MgH_2} - E_{substrate},$$

where $E_{substrate}$ and E_{total} are the total energy of pristine and MgH_2 adsorbed F-Ti_3C_2, respectively. E_{MgH_2} is the energy for MgH_2 molecule. Therefore, a lower value of E_b indicates a stronger adsorption interaction.

Material characterizations

Powder X-ray diffraction (XRD, D8 Advance, Bruker AXS) was used to characterize the crystalline structures of samples with Cu K_α radiation. Amorphous tape covered the samples to prevent any possible reactions between air and samples during the XRD measurement. To determine the morphology and composition of samples, field-emission scanning electron microscopy (FE-SEM; JEOL 7500FA, Tokyo, Japan) and transmission electron microscopy (TEM; JEOL 2011F, Tokyo, Japan) coupled with an energy dispersive spectrometer (EDS) were used. To avoid oxidation of samples before SEM and TEM measurements, samples were firstly dispersed on electrically conducting adhesive tapes and Cu grids, respectively, in a gloves box and then rapidly transferred into the chambers for tested within a few seconds. The X-ray photoelectron spectra (XPS) results were obtained on a Perkin Elmer PHI 5000C ESCA system equipped with a dual X-ray source, in which the Mg K_α anode and a hemispherical energy analyzer was adopted. The background pressure during measurements was maintained below 10^{-6} Pa, and all the measurements were conducted at a pass energy of 93.90 eV. All binding energies were calibrated using contaminant carbon (C 1*s* = 284.6 eV).

Electrode fabrication

The electrochemical performances of all investigated materials were evaluated via CR2032 coin-type half-cell with a pure lithium foil as both the reference and counter electrode. The electrolyte was consisted with 1 M $LiPF_6$ in a mixture solution of EC:EMC:DEC (1:1:1, *v*/*v*/*v*). Celgard 2340 was used as separator. The working electrodes were fabricated by mixing active materials, acetylene black and PMMA binder with a weight ratio of 7:2:1 in *N*,*N*-dimethylformamide (DMF) to form a slurry. Then, the slurry was coated onto nickel foam, and the mass loading of anodes in this work was around 0.5–0.8 mg cm^{-2}. Finally, the anodes were dried in a vacuum oven at 70 °C for 24 h. The coin-type cells were assembled in an Ar-filled glove box with concentrations of moisture and O_2 contents below 0.1 ppm. The specific capacities of nMH/MXene electrode were calculated based on the total volume of nMH/MXene composite. The detailed calculation of volume capacity is shown in Supplementary Information.

Electrochemical measurements

A CHI660D electrochemistry workstation was used to test the cyclic voltammetry (CV) in potential range of 0.001–3 V (vs. Li^+/Li) at a scan rate of 0.1 mV s^{-1} and electrochemical impedance spectroscopy (EIS) from 100 kHz to 0.01 kHz at room temperature. The cycling stability and rate performance were evaluated by a Land Battery Test System in 0.001–3 V (vs. Li^+/Li). Electrodes at different cycling states were washed with DMC in glove box under argon atmosphere, and then dried in vacuum for overnight. Samples collected from dried electrodes were further investigated by TEM.

Results and discussion

In order to investigate the adsorption of MgH_2 on MXene, DFT calculations are performed and various adsorption configurations of MgH_2 are computed. Given that the surface functional groups

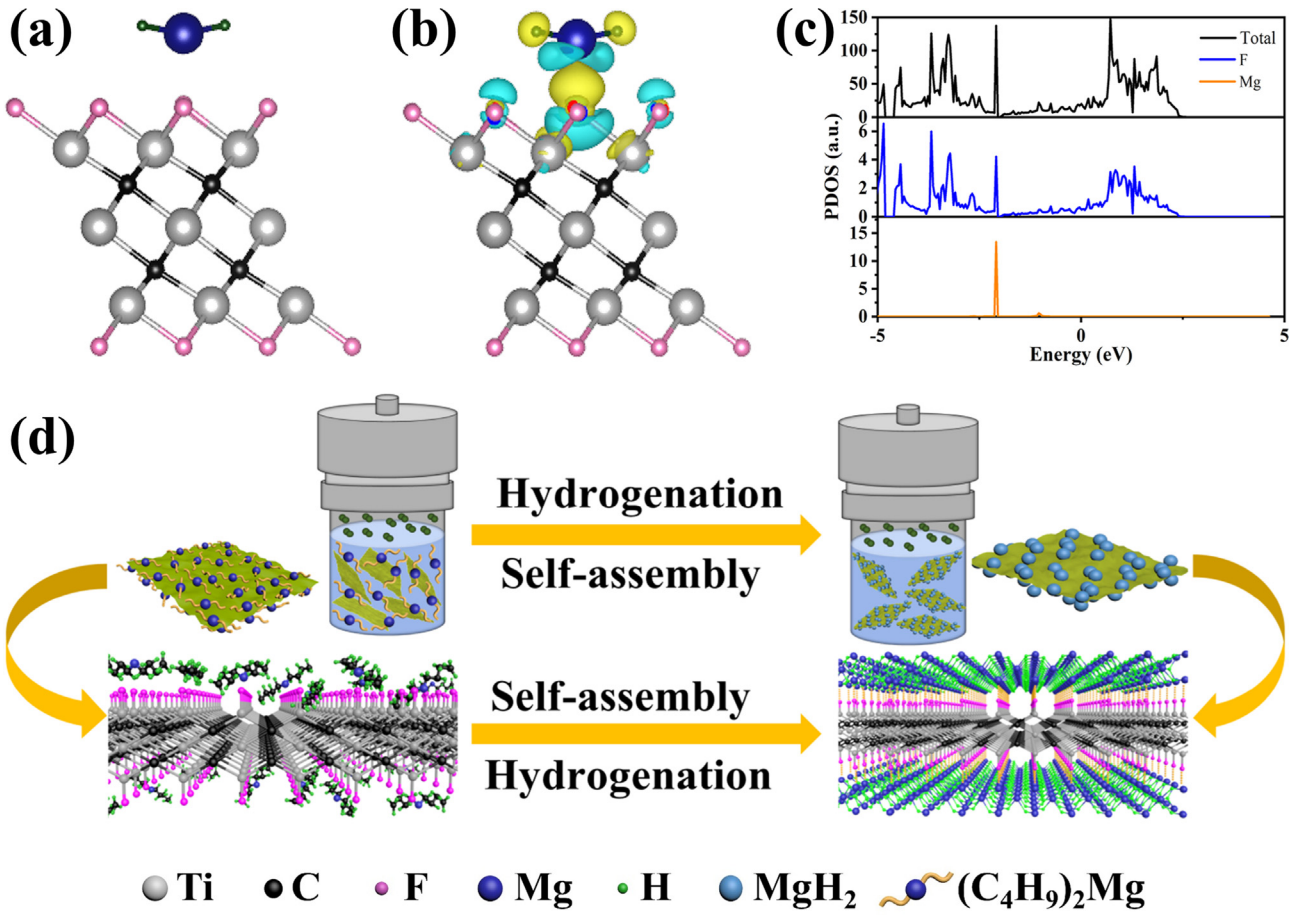

Fig. 1. (a) Adsorption configuration, (b) charge density difference plot and (c) PDOS of MgH_2 adsorbed F-Ti_3C_2. (d) Schematic illustration of nMH self-assembly on the MXene.

will significantly affect the surface properties, fluorine functionalized Ti_3C_2 (denote as F-Ti_3C_2) is firstly used as substrate to adsorb MgH_2. As shown in Fig. 1(a), MgH_2 molecule is adsorbed on the top of F atoms without any distortion. A binding energy of –0.35 eV suggests that the adsorption is favorable thermodynamically. Fig. 1(b) illustrates the charge redistribution of MgH_2 adsorbed on F-Ti_3C_2. The electron accumulation between Mg and F atom suggests the formation of F–Mg bounding. This covalent hybridization interaction is also supported by the projected density of states (PDOS) as plotted in Fig. 1(c), in which the states of Mg and F overlap at ~–2 eV. Compared to F-Ti_3C_2, pristine Ti_3C_2 and HO-Ti_3C_2 couldn't adsorb MgH_2 molecule owing to the fact that the decomposition of MgH_2 molecule is observed as indicated by the break of Mg–H bonds in Fig. S1. Therefore, the existence of F functional groups is the key to realize a strong adsorption of MgH_2 on MXene. Fig. S3 and Table S2 show the variation of Ti, C, O, F, Mg elements. For pristine MXene sheets, the content of F atom is between 12.00% and 13.56%. In the meanwhile, the content of F atom reduces with the decrease of MXene ratio in the nMH/MX-60 sample. Nevertheless, the contents of F are still as high as 4.15% and 5.11% (Fig. S3e, f and Table S2).

According to the results of DFT calculations, the nMH/MX composites with various loading content of MgH_2 were synthesized by simple solvothermal method [40] and the schematic illustration of the MgH_2 self-assembly on MXene is shown in Fig. 1(d). The raw materials used by different nMH/MX composites were displayed in Table Sl. Briefly, a suspension of Ti_3C_2-MXene sheets, synthesized via clay method [25] that etched MAX (Fig. S5a) by LiF/HCl mixtures, were firstly freeze dried and calcined. As shown in Fig. S2, the calcined MXene flakes presented smooth surface, and F atoms were uniformly distributed on MXene according to the elemental mapping. Afterward, the calcined MXene sheets were mixed with dibutyl magnesium ($(C_4H_9)_2Mg$) and cyclohexane (C_6H_{12}). Finally, the nMH/MX composites were obtained through hydrogenating the mixture under 200 °C at 4.5 MPa with followed drying at 70 °C via dynamic vacuum on a Schlenk line.

Fig. 2(a) shows the XRD patterns of MXene, nMH and nMH/MX composites. For the MXene sample, three diffraction peaks attributed to (002), (004) and (008) lattice plane of MXene are clearly observed. In the meanwhile, no characteristic peaks belonging to MAX (Fig. S5a) appeared in the MXene patterns, indicating that Al atoms have been selectively removed during the exfoliation process. For the nMH/MX composites, the diffraction peaks of MXene and nMH were co-existed in the corresponding XRD patterns. In addition, the signal of characteristic peaks of nMH becomes stronger with the increase of the nMH loading content. No additional characteristic peaks appeared in all the patterns, suggesting the high purity of the measured samples. It should be noted that only MgO can be obtained when the MXene sheets without calcination is used to load MgH_2 particles (Fig. S5b). Therefore, the MXene sheets should be calcined to remove its interlayer water and –O, –OH functional groups before preparing nMH/MX samples. As shown in the EDS (Fig. S3a and c) and XPS (Fig. S3b and d, and Table S2) characterization, after calcination, the contents of oxygen declined from 22.46% and 7.24% to 22.50% and 7.06%, respectively. It is noted that the increased content of oxygen in the nMH/MX-60 sample was caused by the oxidation of MgH_2 during test.

To further confirm the absorption of nMH on MXene sheets by F atom. XPS was used to test the valance state of Mg and F atom in the nMH/MX-60 sample. The high-resolution Mg 2*p* and F 1*s* core-level XPS spectra are shown in Fig. 2(b and c). The Mg 2*p* spectrum (Fig. 2b) demonstrates peaks at 49.8, 50.9, and 51.8 eV,

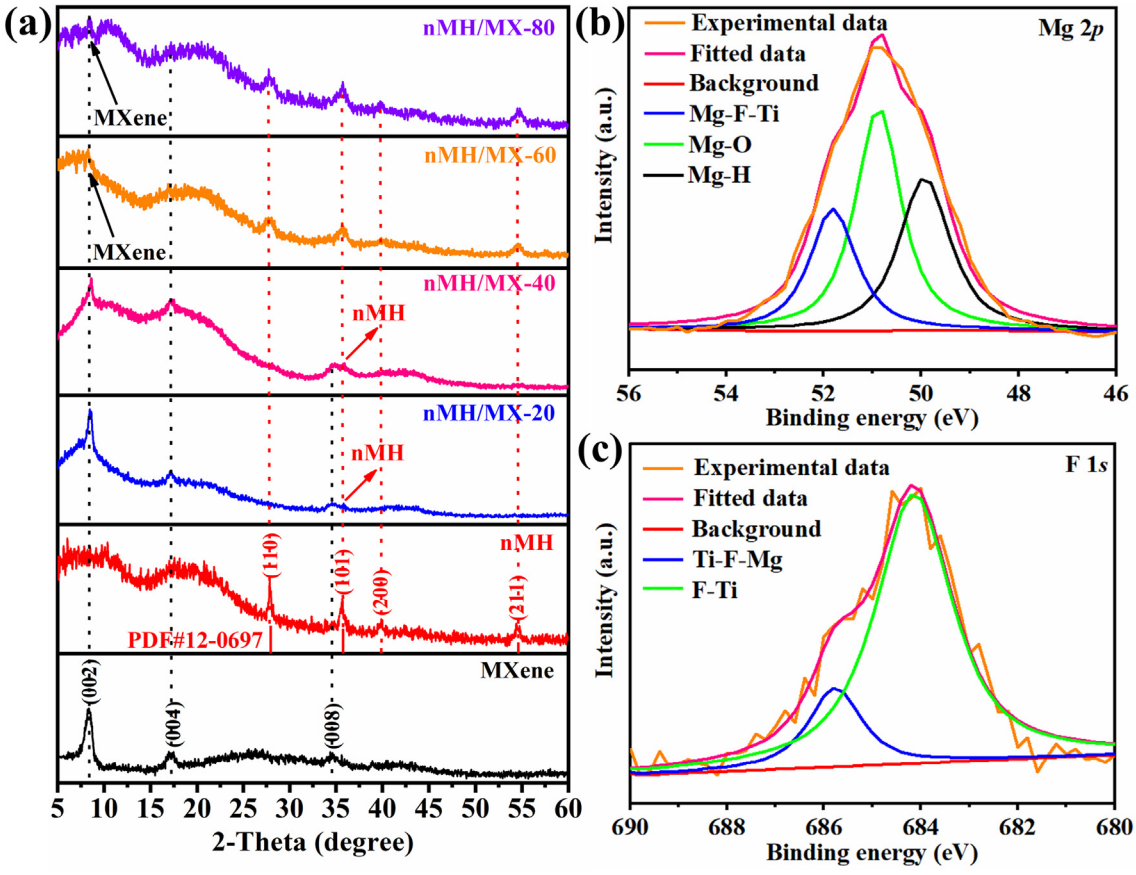

Fig. 2. (a) XRD patterns of MXene, nMH, and nMH/MX composites. (b) Mg 2*p* and (c) F 1*s* XPS spectra of nMH/MX-60.

respectively. Meanwhile, the F 1*s* spectrum (Fig. 2c) shows peaks at 685.7 and 684.2 eV, respectively. The peak at 49.8 eV can be ascribed to the signal of Mg–H. The peak at 50.9 eV corresponds to Mg–O, which may be formed during the test process. The peaks at 51.8 and 685.7 eV are attributed to the signals of F–Mg, which illustrate the adsorption of F-Ti_3C_2 to nMH. The Mg 2*p* spectrum of pristine MgH_2 nanoparticles has been shown in Fig. S4. Only Mg–H and Mg–O signals can be observed, which further support the existence of F–Mg bounding in the nMH/MX-60 sample. It is well known that the abundant surface/interface issue is critical for the correlated battery performance [41]. The formed F–Mg bounding will strengthen the interface properties between MXene and MgH_2 and then affect the electrochemical performance. The peak at 684.2 eV belonging to F–Ti is derived from the F functional group in MXene.

The FESEM and TEM images are shown in Fig. 3, which display the distribution of nMH on the surface of MXene sheets. Fig. 3(a–d) show the SEM images of nMH/MX composites with different nMH content from 20 to 80 wt%. It can be seen that nMH are homogeneously distributed on the MXene sheets under the function of F–Mg bounding for all the samples. In the meanwhile, MgH_2 particles on the surface of MXene are enriched with the increase of loading ratio. When the MgH_2 content reaches to 60 wt%, MgH_2 particles on the surface of MXene have been accumulated layer by layer (Fig. 3c) owing to the limited surface area of MXene. Therefore, the newly increased MgH_2 particles in the nMH/MX-80 sample will continue to accumulate, which leads to the more excessive accumulation of nMH on the MXene sheets. The same condition can be observed from the corresponding TEM images (Fig. 3e–h), which illustrate the content of nMH could be easily adjusted via changing the dosage of Mg precursor. The high-resolution TEM (HRTEM) pattern (Fig. 3i) indicates that the well-crystallized nature of nMH with distinct lattice fringes that attribute to the (200) planes of MgH_2 with a d-spacing of 2.23 Å. The selected-area electron diffraction (SAED) image (insert of Fig. 3i) further verifies that the crystallized nMH were displayed polycrystalline structure, which is agreed to the XRD results. In the meanwhile, the distinct lattice fringes of MXene with a d-spacing of 1.16 nm attributed to (200) planes could be observed in Fig. S6, which is agreed with the XRD results that the diffraction peaks of (200) planes of MXene appear at 2-theta of 7.94°. The well dispersed nMH on MXene sheets were further illustrated by the STEM (Fig. 3j) and the corresponding Ti, C, Mg elemental mapping.

The galvanostatic charge/discharge test was used to systematically investigate the electrochemical performance of nMH/MX electrodes. All specific capacities were tested based on the weight of composites. Fig. 4(a) presents the cycling stability of nMH/MX composites with nMH content ranging from 20 to 80 wt% at a current density of 100 mA g^{-1}, which shows that the electrochemical performance of electrodes were depended on the content of nMH. The initial capacities of 629.5, 792.2, 1051.2 and 830.4 mAh g^{-1} were provided by nMH/MX electrodes with the nMH content from 20 to 80 wt%, respectively. Furthermore, the reduction of nMH content was beneficial to improve the cycle stability of composites, in which the nMH/MX-60 sample gives the optimal electrochemical performance, with a gravimetric capacity of 389.3 mAh g^{-1} after 100 cycling at 100 mA g^{-1}. In addition, the nMH/MX-60 sample also provides the best rate performance as shown in Fig. 4(b). It

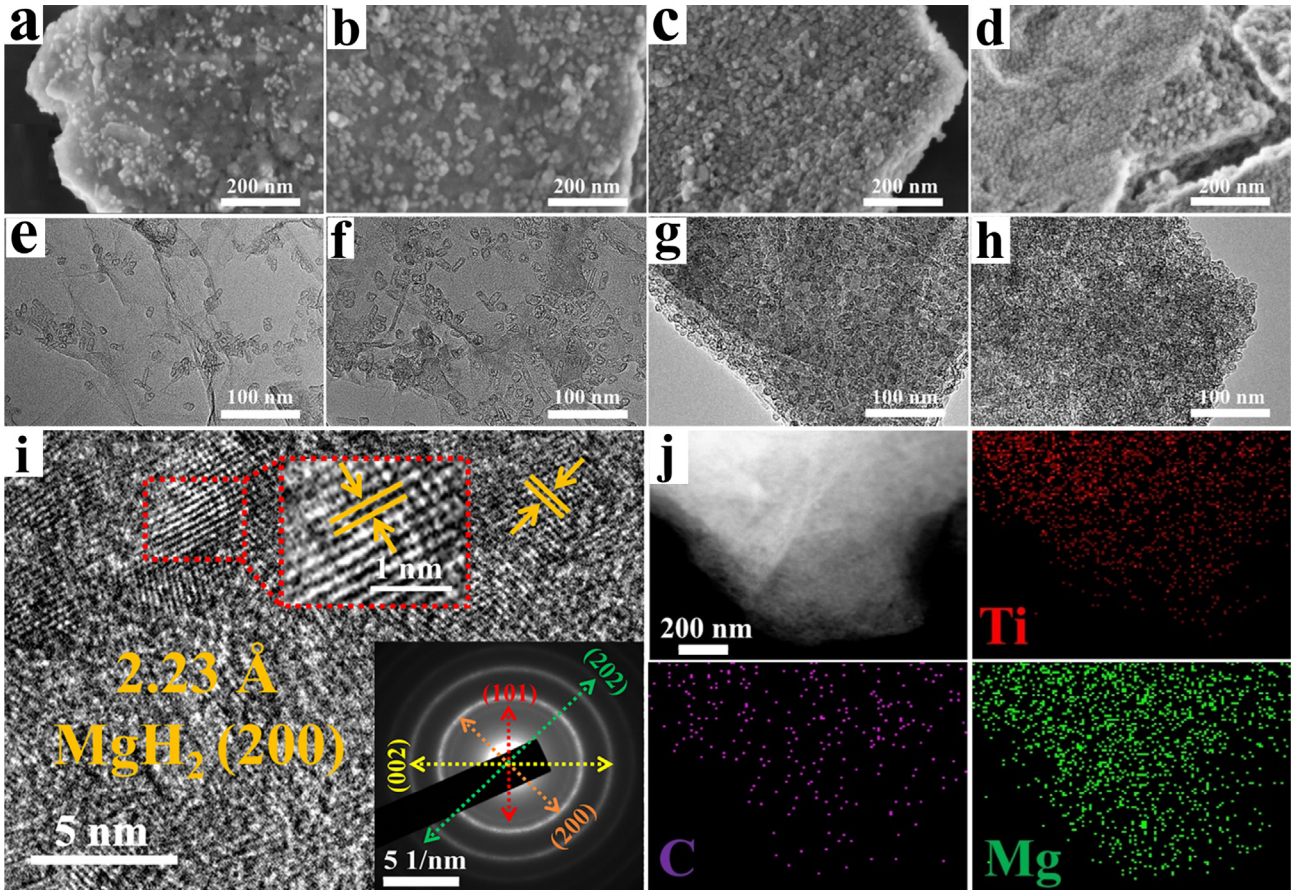

Fig. 3. (a–d) SEM images, (e–h) TEM images of nMH/MX-20, nMH/MX-40, nMH/MX-60 and nMH/MX-80, respectively. (i) HRTEM image of nMH/MX-60. The inset shows the corresponding SAED image and enlarge picture of the red box area. (j) STEM image and the corresponding elemental mapping of Ti, Mg and C of nMH/MX-60.

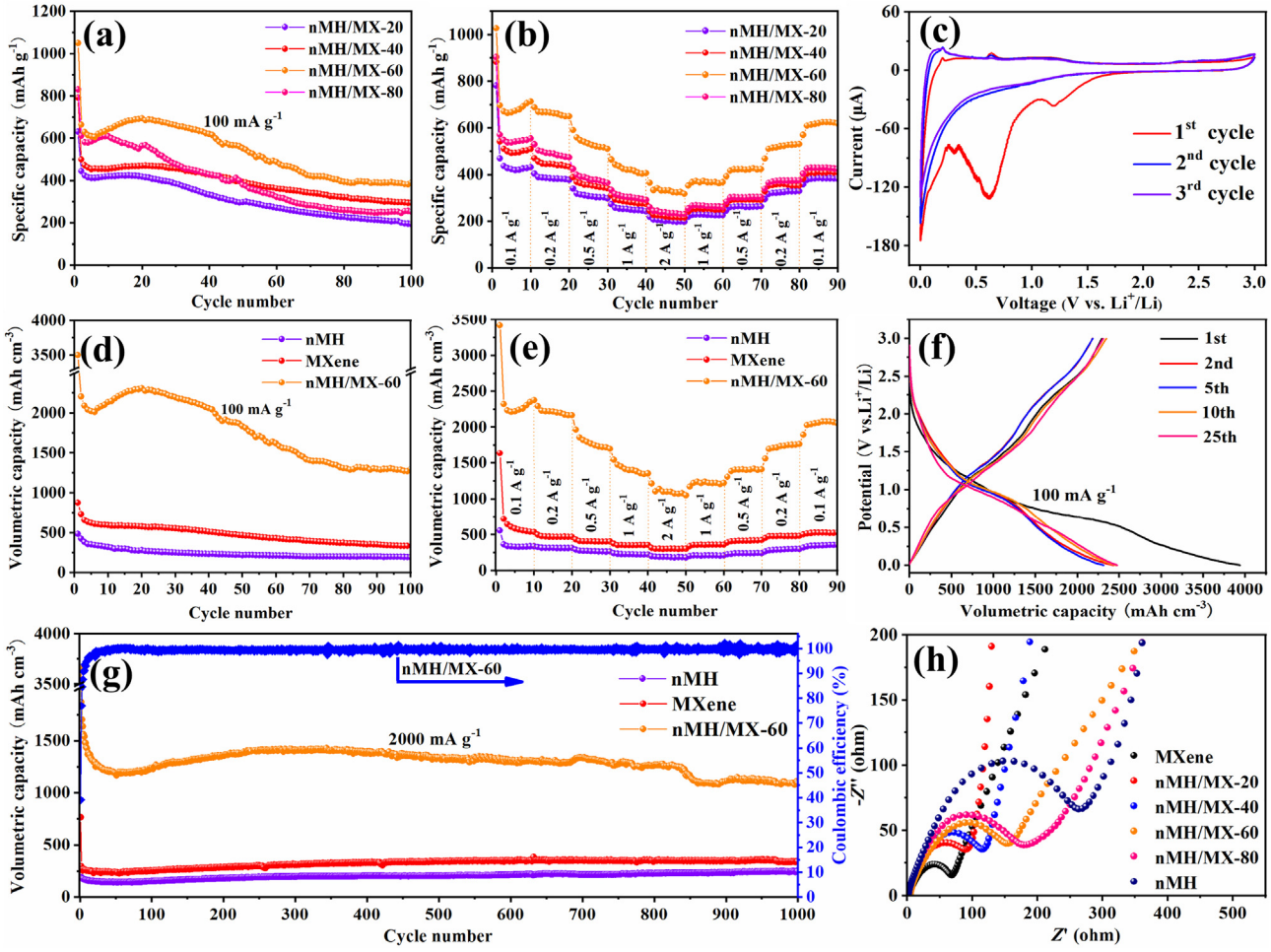

Fig. 4. (a) Cycling performances of nMH/MX electrodes with different nMH content at 100 mA g^{-1}. (b) Rate capacities of nMH/MX electrodes with different nMH contents at varied current rates from 100 to 2000 mA g^{-1}. (c) CV curves of nMH/MX-60 at a scan rate of 0.1 mV s^{-1} for the first three cycles. Cycling performances of MXene, nMH and nMH/MX-60 electrodes at a current density of (d) 100 and (g) 2000 mA g^{-1}, respectively. (e) Rate capacities of MXene, nMH and nMH/MX-60 electrodes at different current rates from 100 to 2000 mA g^{-1}. (f) Discharge/charge profiles of nMH/MX-60 at different cycles under 100 mA g^{-1}. (h) EIS of the MXene, nMH/MX-20, nMH/MX-40, nMH/MX-60, nMH/MX-80 and nMH electrodes from 100 to 0.01 kHz before cycled. All capacity was tested in the voltage range of 0.001–3 V (vs. Li^+/Li).

delivers an average capacity of 328.0 mAh g^{-1} at a current density of 2000 mA g^{-1}. The fact that the capacity of nMH/MX-80 declined sharply and is ultimately less than that of nMH/MX-40 and nMH/MX-60 samples after 100 cycles is owing to the excessive accumulation of nMH on the MXene sheets. The above results demonstrate that the MXene sheets are able to buffer the volume expansion, improve the conductivity of the battery system, and avoid the shedding of nMH from composite to electrolyte. To further demonstrate the positive effect of MXene on the MgH_2 electrode, 60 wt% commercial MgH_2 ball milled with MXene (cMH/MXene-60) and Super P (cMH/C-60) were prepared and the cycling and rate performances are shown in Fig. S8. The enhanced lithium storage capacity and rate performance of cMH/MXene-60 compared to cMH/C-60 demonstrated that MXene matrix is benefit to improve the lithium storage performance of MgH_2 compared with the Super P. However, the fact that the cMH/MXene-60 electrode was sharply declined during the first five cycles suggests the limitation of MXene on improving the MgH_2 electrode with large particle size (Fig. S10), which further confirms the superiority of the nanosized MgH_2 anchored on MXene sheets synthesized by solvothermal method in this study.

The discharge/charge process of MgH_2 toward lithium storage has been wildly explored and reported as following formulas [14,18]:

$$MgH_2 + 2Li^+ + 2e^- \leftrightarrow Mg + 2LiH \quad (1)$$

$$Mg + xLi^+ + xe^- \leftrightarrow Li_xMg \quad (2)$$

To better understand the electrochemical route of nMH/MX electrode, CV was performed for nMH/MX-60 sample to monitor within a voltage window of 0.001–3 V at a scan rate of 0.1 mV s^{-1} (Fig. 4c). Similar to the reported literature, the initial cathodic CV profile is different with subsequent discharge curves [23,42]. The broad negative peaks disappeared in subsequent cycles originate at approximately 1.5 V in the first cycle, which is likely ascribed to the formation of SEI film. The reduction peak stared at 0.3 V is attributed to the cathodic lithiation of MgH_2 to form Li_xMg, and the two oxidation peaks detected at 0.2 and 0.62 V correspond to the dealloying of Li_xMg and the regeneration of MgH_2, respectively. In the subsequent cycles, the CV curves are well overlapped, which demonstrate the good reversibility of nMH/MX-60 electrodes in the electrochemical process. The obtained CV profiles are consistent with the charge/discharge behaviors of nMH/MX-60 composite (Fig. 4f), for which the profiles in the first 25 cycles are highly overlapped and exhibit a slant plateau at the corresponding voltage.

Given that MXene has the potential to supply a high volumetric energy density due to its natural high density, the volumetric

capacities of the nMH/MX-60 electrode were also tested as show in Fig. 4(d). It presents an initial discharge/charge capacity of 3500.6 and 2071.8 mAh cm^{-3}, respectively. The irreversible charge capacity of around 40% at the first cycle is largely caused by the inevitable formation of SEI film. Clearly, to solve this problem, modifying the surface of MgH_2 particles with a layer of polythiophene conductive polymer is an effective method, which can alleviate the volume expansion and protect MgH_2 particles from side reactions [24]. As a comparison, the discharge capacities of the pristine MXene and nMH are only 876.0 and 486.3 mAh cm^{-3}. The significant improvement in the volumetric capacities of nMH/MX-60 electrode is attributed to the inherent high density of MXene and the improved capacity contribution of nMH. In the subsequent cycles, the capacity of nMH/MX-60 increased in the first 20 cycles due to the activation of electrode, and then slowly reduced. After 100 cycles, the nMH/MX-60 electrode could deliver a reversible capacity of 1296.3 mAh cm^{-3} much higher than that of MXene (333.0 mAh cm^{-3}) and nMH (193.1 mAh cm^{-3}). Moreover, the nMH/MX-60 electrode also exhibited a superior rate performance as shown in Fig. 4(e). The average capacities are 2292.4, 2209.6, 1783.6, 1412.3, and 1104.4 mAh cm^{-3} at 100, 200, 500, 1000 and 2000 mA g^{-1}, respectively. When the current density returns to 100 mA g^{-1} after high-rate cycling, the capacity could restore to 2044.0 mAh cm^{-3}, confirming its good reversibility. As a result, a high capacity of 1092.9 mAh cm^{-3} with a Coulombic efficiency of 99.5% at a high rate of 2000 mA g^{-1} is achieved for the nMH/MX-60 electrode after 1000 cycles (Fig. 4g). In summary, nMH/MX-60 anode is comparable to other reported MgH_2 anodes in gravimetric capacity and cyclability (Fig. S9) [18,20–23,43]. More importantly, benefiting to the high density of MXene sheets, the nMH/MX-60 can provide 3–6 times volumtric capacity compared with other MgH_2 anodes (Fig. 4).

EIS was used to explore the kinetics of electrode materials. The Nyquist plots of MXene, nMH/MX-20, nMH/MX-40, nMH/MX-60, nMH/MX-80, and nMH were compared at Fig. 4(h) by fresh cells at the frequency ranging from 100 kHz to 0.01 Hz. All six Nyquist polts contain a depressed semicircle at high and medium frequency and an inclined line at low frequency. With the increasing of MXene content, the diameter of the semicircle of samples gradually diminishes. In the meanwhile, the diffusion coefficients of MXene, nMH/MX-20, nMH/MX-40, nMH/MX-60, nMH/MX-80 and nMH are calculated to be 8.25×10^{-15}, 5.25×10^{-15}, 4.62×10^{-15}, 2.61×10^{-15}, 1.26×10^{-15} and 1.20×10^{-15} cm^2 s^{-1}, respectively, which indicates that MXene can significantly enhance the conductivity of composites, leading to the significantly improved electrochemical performance of nMH/MX composites.

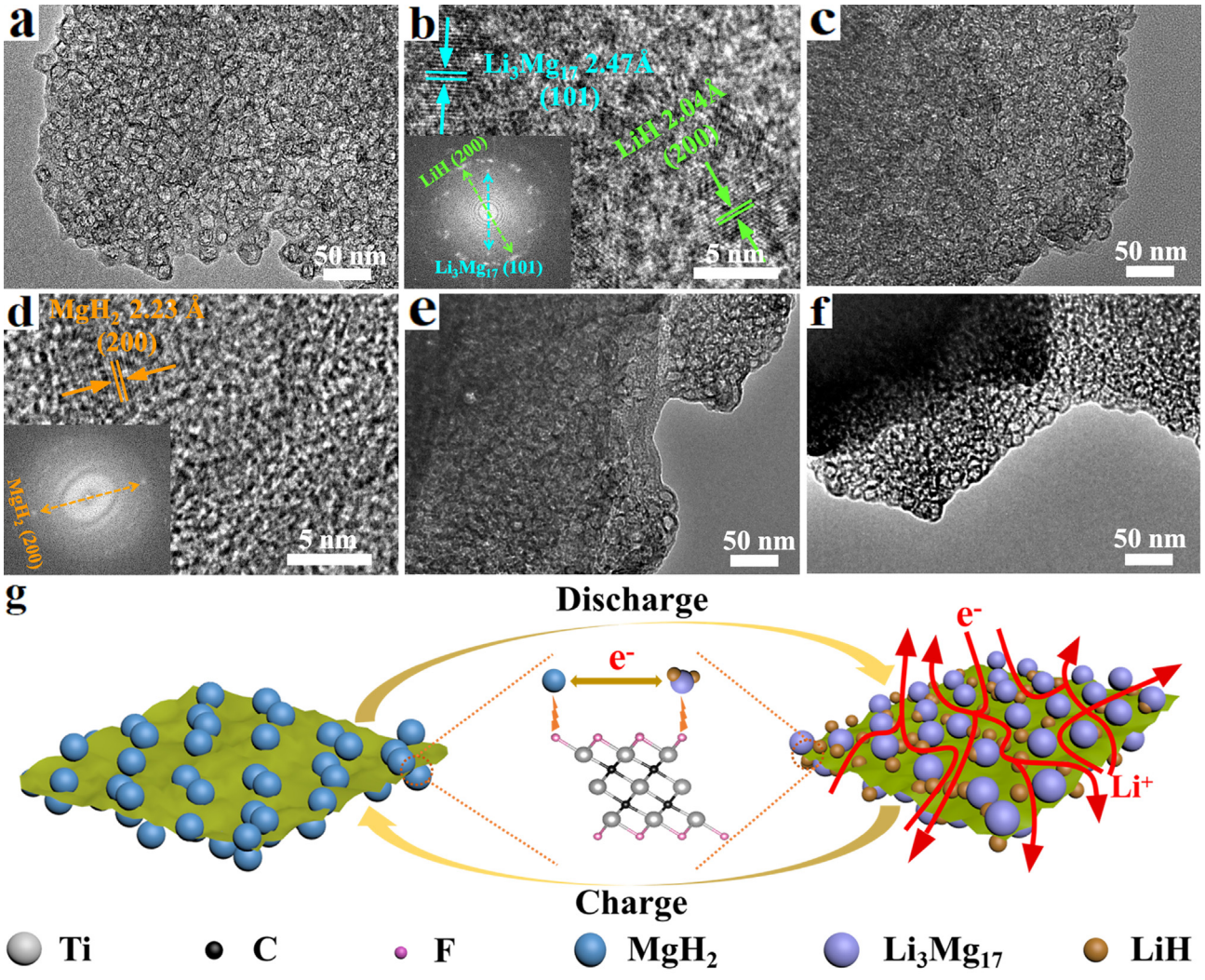

Fig. 5. (a) TEM image, (b) HRTEM image of nMH/MX-60 at 1st fully discharged. (c) TEM image, (d) HRTEM image of nMH/MX-60 at 1st fully charged. The inserts of (b and d) are the corresponding SAED and FFT patterns. TEM images of nMH/MX-60 at (e) 20th and (f) 50th fully discharged/charged. (g) Schematic illustration the advantages of MXene matrix for improved lithium storage of magnesium hydride.

The stability of electrodes was further confirmed through monitoring the morphology variation of nMH with and without MXene matrix during cycling by TEM. Fig. 5(a and b) show the TEM and HRTEM images of nMH/MX-60 after totally discharged to 0.001 V. There are two different nanocrystals that correspond to the lattice fringes with d-spacing of 2.04 and 2.47 Å marked to the (200) and (101) lattice plane of LiH and Li_3Mg_{17}, respectively. When the electrode was fully charged back to 3.0 V, the lattice plane (200) of nMH nanocrystal with d-spacing of 2.23 Å could be detected as displayed at Fig. 5(d). These characteristics can be further confirmed by the SAED and fast Fourier transform (FFT) patterns (insert of Fig. 5b and d). After 20th and 50th cycles, the morphologies of electrodes are well kept (Fig. 5e and f), which demonstrate the preeminent stability of the integrated structure of nMH/MX-60. As a contrast, nMH were significantly cracked and agglomerated after 20 cycles compared to the fresh nMH (Fig. S11). The great change of nMH in morphology during cycling is due to the huge volume expansion, which leads to the continual reformation of SEI film and further rapid capacity decline. The different morphology and structure between the samples of nMH with and without MXene after cycling indicate the synergistic effects of MXene matrix on improving the cycle stability of nMH. As illustrated in Fig. 5(g), the MXene sheets are able to provide rapid electrons and ions transportation pathway and the flexible 2D structure of MXene sheets could sufficiently buffer the volume change of nMH upon cycling. More importantly, the F–Mg bounding between MgH_2 and MXene could effectively restrict the nMH anchored on MXene sheets and further avoid the shedding of nMH during repeated lithium insertion/extraction process.

Conclusions

In summary, we report the synthesis of monodisperse nMH with an average size of < 20 nm uniformly anchored on flexible MXene sheet by a simple solvothermal method. The uniformly dispersed nMH can not only enhance both the electrons and lithium ions transport kinetics of the whole electrode, but also relieve the strain caused by its volume change during the charge/discharge process. Moreover, MXene sheets served as a support to load monodisperse nMH, can provide a fast pathway for electrons/lithium ions transport, play as a flexible substrate for alleviating the volume change during cycling, and maintain the attachment of nMH on MXene attributing to the formed F–Mg bounding. As a result, the nMH/MX composites exhibit outstanding lithium storage performance with high Coulombic efficiency, enhanced stability, favorable rate performance, and improved reversible capacity. More importantly, the nMH/MX composites could deliver distinguished volumetric capacities owing to the natural high density of MXene. As a consequence, reversible capacities of 1296.4 mAh cm^{-3} at 100 mA g^{-1} after 100 cycles and 1092.9 mAh cm^{-3} at 2000 mA g^{-1} after 1000 cycles were obtained for the nMH/MX-60 composite, enabling it a promising anode material for LIBs with high capacity.

Declaration of Competing Interest

The authors declare that they have no known competing financial interests or personal relationships that could have appeared to influence the work reported in this paper.

Acknowledgments

This work was partially supported by the National Science Fund for Distinguished Young Scholars (51625102), the National Natural Science Foundation of China (51971065), the Innovation Program of Shanghai Municipal Education Commission (2019–01–07–00–07–E00028), and the Open Fund of Jiangsu Key Laboratory of Electrochemical Energy Storage Technologies No. EEST2019–2.

Appendix A. Supplementary data

Supplementary data to this article can be found online at https://doi.org/10.1016/j.jechem.2021.03.049.

References

[1] N.A. Kaskhedikar, J. Maier, Adv. Mater. 21 (2009) 2664–2680.
[2] G. Xia, H. Zhang, M. Liang, J. Zhang, W. Sun, F. Fang, D. Sun, X. Yu, Adv. Mater. 31 (2019) 1901372.
[3] H. Zhang, X. Huang, O. Noonan, L. Zhou, C. Yu, Adv. Funct. Mater. 27 (2017) 1606023.
[4] C.K. Chan, H. Peng, G. Liu, K. McIlwrath, X.F. Zhang, R.A. Huggins, Y. Cui, Nat. Nanotechnol. 3 (2008) 31–35.
[5] Y. Tian, Y. An, J. Feng, ACS Appl. Mater. Interfaces 11 (2019) 10004–10011.
[6] J. Wang, W. Li, F. Wang, Y. Xia, A.M. Asiri, D. Zhao, Nanoscale 6 (2014) 3217–3222.
[7] Y. Wang, Y. Li, Z. Qiu, X. Wu, P. Zhou, T. Zhou, J. Zhao, Z. Miao, J. Zhou, S. Zhuo, J. Mater. Chem. A 6 (2018) 11189–11197.
[8] J. Liu, M. Gu, L. Ouyang, H. Wang, L. Yang, M. Zhu, ACS Appl. Mater. Interfaces 8 (2016) 8502–8510.
[9] X. Wu, Z. Wang, M. Yu, L. Xiu, J. Qiu, Adv. Mater. 29 (2017) 1607017.
[10] C. Wang, H. Xie, S. Chen, B. Ge, D. Liu, C. Wu, W. Xu, W. Chu, G. Babu, P.M. Ajayan, L. Song, Adv. Mater. 30 (2018) 1802525.
[11] C. Wang, S. Chen, H. Xie, S. Wei, C. Wu, L. Song, Adv. Energy Mater. 9 (2019) 1802977.
[12] J. Choi, W.-S. Kim, K.-H. Kim, S.-H. Hong, J. Mater. Chem. A 6 (2018) 17437–17443.
[13] J. Qin, C. He, N. Zhao, Z. Wang, C. Shi, E.-Z. Liu, J. Li, ACS Nano 8 (2014) 1728–1738.
[14] L. Aymard, Y. Oumellal, J.P. Bonnet, Beilstein J. Nanotechnol. 6 (2015) 1821–1839.
[15] S. Brutti, D. Meggiolaro, A. Paolone, P. Reale, Mater. Today Energy 3 (2017) 53–59.
[16] Z.-S. Wu, W. Ren, L. Xu, F. Li, H.-M. Cheng, ACS Nano 5 (2011) 5463–5471.
[17] B. Gao, X. Li, K. Ding, C. Huang, Q. Li, P.K. Chu, K. Huo, J. Mater. Chem. A 7 (2019) 14–37.
[18] Y. Oumellal, A. Rougier, G.A. Nazri, J.M. Tarascon, L. Aymard, Nat. Mater. 7 (2008) 916–921.
[19] X. Peng, H. Wang, R. Hu, L. Ouyang, J. Liu, M. Zhu, J. Alloys Compd. 711 (2017) 473–479.
[20] S. Brutti, G. Mulas, E. Piciollo, S. Panero, P. Reale, J. Mater. Chem. 22 (2012) 14531–14537.
[21] A. El kharbachi, H.F. Andersen, M.H. Sørby, P.E. Vullum, J.P. Mæhlen, B.C. Hauback, Int. J. Hydrogen Energy 42 (2017) 22551–22556.
[22] Y. Oumellal, C. Zlotea, S. Bastide, C. Cachet-Vivier, E. Léonel, S. Sengmany, E. Leroy, L. Aymard, J.-P. Bonnet, M. Latroche, Nanoscale 6 (2014) 14459–14466.
[23] B. Zhang, G. Xia, D. Sun, F. Fang, X. Yu, ACS Nano 12 (2018) 3816–3824.
[24] G. Xia, B. Zhang, X. Chen, D. Sun, Z. Guo, F. Liang, W. Zou, Z. Yang, X. Yu, ACS Nano 12 (2018) 8177–8186.
[25] M. Ghidiu, M.R. Lukatskaya, M.Q. Zhao, Y. Gogotsi, M.W. Barsoum, Nature 516 (2014) 78–81.
[26] C. Chen, X. Xie, B. Anasori, A. Sarycheva, T. Makaryan, M. Zhao, P. Urbankowski, L. Miao, J. Jiang, Y. Gogotsi, Angew. Chem. Int. Ed. 57 (2018) 1846–1850.
[27] Z. Sun, M. Yuan, L. Lin, H. Yang, C. Nan, H. Li, G. Sun, X. Yang, ACS Mater. Lett. 1 (2019) 628–632.
[28] Z. Ma, X. Zhou, W. Deng, D. Lei, Z. Liu, ACS Appl. Mater. Interfaces 10 (2018) 3634–3643.
[29] M.Q. Zhao, X. Xie, C.E. Ren, T. Makaryan, B. Anasori, G. Wang, Y. Gogotsi, Adv. Mater. 29 (2017) 1702410.
[30] Y. Wu, P. Nie, J. Jiang, B. Ding, H. Dou, X. Zhang, ChemElectroChem 4 (2017) 1560–1565.
[31] Y. Yoon, M. Lee, S.K. Kim, G. Bae, W. Song, S. Myung, J. Lim, S.S. Lee, T. Zyung, K.-S. An, Adv. Energy Mater. 8 (2018) 1703173.
[32] X. Li, C. Wen, H. Li, G. Sun, J. Energy Chem. 47 (2020) 272–280.
[33] C. Wen, T. Zhu, X. Li, H. Li, X. Huang, G. Sun, Chinese Chem. Lett. 31 (2020) 1000–1003.
[34] J.-C. Lei, X. Zhang, Z. Zhou, Front. Phys. 10 (2015) 276–286.
[35] X. Wang, S. Kajiyama, H. Iinuma, E. Hosono, S. Oro, I. Moriguchi, M. Okubo, A. Yamada, Nat. Commun. 6 (2015) 6544.
[36] Z. Ling, C.E. Ren, M.Q. Zhao, J. Yang, J.M. Giammarco, J. Qiu, M.W. Barsoum, Y. Gogotsi, Proc. Natl. Acad. Sci. U.S.A. 111 (2014) 16676–16681.
[37] M. Naguib, M. Kurtoglu, V. Presser, J. Lu, J. Niu, M. Heon, L. Hultman, Y. Gogotsi, M.W. Barsoum, Adv. Mater. 23 (2011) 4248–4253.
[38] J. Luo, X. Tao, J. Zhang, Y. Xia, H. Huang, L. Zhang, Y. Gan, C. Liang, W. Zhang, ACS Nano 10 (2016) 2491–2499.
[39] S. Niu, Z. Wang, M. Yu, M. Yu, L. Xiu, S. Wang, X. Wu, J. Qiu, ACS Nano 12 (2018) 3928–3937.

[40] G. Xia, Y. Tan, X. Chen, D. Sun, Z. Guo, H. Liu, L. Ouyang, M. Zhu, X. Yu, Adv. Mater. 27 (2015) 5981–5988.
[41] W. Zhang, D. Wang, W. Zheng, J. Energy Chem. 41 (2020) 100–106.
[42] Y. Xu, F.M. Mulder, Int. J. Hydrogen Energy 43 (2018) 20033–20040.
[43] W. Zaïdi, Y. Oumellal, J.-P. Bonnet, J. Zhang, F. Cuevas, M. Latroche, J.-L. Bobet, L. Aymard, J. Power Sources 196 (2011) 2854–2857.